Supporting Information:

# Regulating the electronic structure of catalysts via stable ceria and adjustable copper metal/oxide towards efficient overall water splitting

Huan Zheng,[#a] Tao Yin, [#a] Jialong Yu,[a] Wei Xu,[b] Weizhen Zhang,[a] Qihui Yu,[a] Yingnan Guo,[a] Li Guan,*[a] Xiaolei Huang,*[c], Fenghe Wang*[a,]

[a] Hebei Key Laboratory of Photo-Electricity Information and Materials, College of Physics Science and Technology, Hebei University, Baoding 071002, P R China

[b] Beijing Synchrotron Radiation Facility, Institute of High Energy Physics, Chinese Academy of Science, Beijing, 100049, PR China

[c] Key Laboratory of Rare Earths, Ganjiang Innovation Academy, Chinese Academy of Science, Ganzhou, China

[#]H. Z. and T. Y. contributed equally to this work.

***Corresponding Author**

E-mail address: lguan@hbu.edu.cn (L. Guan)

E-mail: xlhuang@gia.cas.cn; x.l.huang@hotmail.com (X. Huang)

E-mail: fenghe_wang@hotmail.com (F. Wang)

## Experimental Section

**Chemicals:** $Co(NO_3)_2 \cdot 6H_2O$, $Cu(NO_3)_2 \cdot 3H_2O$, $Ce(NO_3)_3 \cdot 6H_2O$, $C_{15}H_{34}BrN$ were acquired from Aladdin Industrial Co., Ltd. $CH_3OH$ was required from Comiou Reagent Co., Ltd. KOH was purchased from Fuchen (Tianjin) Chemical Reagent Co., Ltd. The reagents were utilized without additional purification.

**Synthesis of Co-NS:** A solution containing 0.036 M of $Co(NO_3)_2 \cdot 6H_2O$ was prepared by dissolving it in 50 mL of deionized water. The carbon cloth that underwent treatment was utilized as the working electrode, while the Pt wire served as the counter electrode, and the saturated calomel electrode functioned as the reference electrode. The three-electrode setup was submerged in the $Co(NO_3)_2 \cdot 6H2O$ solution. The chronopotentiometry approach was employed to set the operating voltage to -0.98 V (vs. RHE) for 360 seconds. The sample was dried at a temperature of 60°C for a duration of 720 minutes after being washed, resulting in the formation of Co-NS.

**Synthesis of CoCu-NS:** Dissolve 0.241 g copper nitrate in 25 mL deionized water and stir thoroughly. Co-NS was placed in a solution at an ambient temperature of 25 °C and impregnated for 120 minutes. CoCu-NS was produced by the process of natural drying once it was finished

**Synthesis of CoCuCe-NS:** A solution was prepared by dissolving 0.06 M $Ce(NO_3)_3 \cdot 6H_2O$ and 0.01 M $C_{15}H_{34}BrN$ reagents in 50 mL of methanol, followed by stirring until complete dissolution. Subsequently, a three-electrode system consisting of CoCu-NS, graphite paper, and

Ag/AgCl as was immersed in the solution and deposited at a current density of -20 mA $cm^{-2}$ for 3 minutes. Wash after finishing and dry naturally to obtain CoCuCe-NS.

**Synthesis of CoCe-NS:** The preparation of CoCe-NS is similar to that of CoCuCe-NS. Co-NS as a working electrode was inserted into a mixed solution containing $Ce(NO_3)_3 \cdot 6H_2O$ and $C_{15}H_{34}BrN$ regrants, other conditions remained unchanged.

**Physical characterizations of prepared catalysts**

The morphology of samples was determined by scanning electron microscopy (SEM, FEI Nova NanoSEM450, 10 kV) and high-resolution transmission electron microscopy (HRTEM, JEOL-2100Plus, 200 kV). The HAADF images, EDX mapping, and structural information of the sample morphology were completed by spherical aberration-corrected transmission electron microscopy (AC-TEM) equipment (Thermo Scientific Themis Z), and the acceleration voltage was 200 kV. Crystal structural analysis was conducted using X-ray diffraction (XRD) with a D8 ADVANCE instrument. To further verify the structural information and chemical compounds, X-ray photoelectron spectroscopy (XPS, ESCALab250Xi, Thermo) was used. The Raman spectroscopy was performed on materials using a Horiba HR Evolution system instrument with a wavelength of 532 nm.. The underwater bubble contact Angle was completed by Lauda Scientific LSA100. The Co and Cu L2,3-edge X-ray absorption spectra (XAS) of the samples were measured at the 4B9B beamline at the Beijing Synchrotron Radiation Facility (BSRF).

**Electrochemical characterizations**

Electrochemical measurements are conducted at ambient temperature using a multi-channel electrochemical workstation (Biologic, VMP-3). A conventional three-electrode system was used for testing in 1M KOH solution, consisting of the prepared sample as the working electrode, graphite paper as the counter electrode, and Hg/HgO as the reference electrode. The entire overpotential was transformed into reversible hydrogen electrodes (RHE) using the following formula:

$$E_{(RHE)}=0.059*pH+0.098+E_{(Hg/HgO)} \quad (1)$$

Polarization curves for the hydrogen evolution reaction (HER) and oxygen evolution reaction (OER) were produced using linear sweep voltammetry (LSV) at a scanning rate of 1 mV $s^{-1}$, with 85% ohmic resistance (iR) correction. The electrochemical impedance spectra (EIS) were obtained at an external bias of 0.7 V and the frequency range was 700 KHz-100 mHz. The double layer capacitance ($C_{dl}$) is determined using cyclic voltammetry using various sweep speeds during the non-Faraday region in order to evaluate the electrochemical active area (ECSA).

$$ECSA=C_{dl}/C_s \quad (2)$$

Where Cs represents the specific capacitance. The capacitance value of a metal oxide with a flat surface is 0.04 mF·$cm^{-2}$.[1]

**Theoretical calculation method**

OER calculation: The projector augmented wave (PAW) is implemented using the Vienna ab initio Simulation Package (VASP) software inside the density functional theory (DFT) framework. In this case, the Perdew−Burke−Ernzerhof (PBE) algorithm is used to compute the exchange-correlation energy function. A cutoff energy of 500 eV is used for all calculations.

The equilibrium lattice constants of CoOOH, CuO-CoOOH, and $CeO_2$-CoOOH were optimized. The k points of the Brillouin zone are 2×1×1, and the vacuum layer thickness of all slab models is maintained at 15 Å. Geometrically optimized energies converge to $10^{-5}$ eV and forces converge to 0.05 eV $Å^{-1}$

The activity of the oxygen evolution reaction was evaluated using the four-electron mechanism proposed by Nørskov and collaborators:[2-4]

*(1)* $H_2O\ (l) + * \rightarrow OH^* + H^+ + e^-$

$$\Delta G_1 = E_{OH*} - E_* + 1/2 \cdot E(H_2) - E(H_2O) + \Delta E_{ZPE} - T\Delta S \quad (3)$$

*(2)* $HO^* \rightarrow O^* + H^+ + e^-$

$$\Delta G_2 = E_{O*} - E_{OH*} + 1/2 \cdot E(H_2) + \Delta E_{ZPE} - T\Delta S \quad (4)$$

*(3)* $O^* + H_2O\ (l) \rightarrow OOH^* + H^+ + e^-$

$$\Delta G_3 = E_{OOH*} - E_{O*} + 1/2 \cdot E(H_2) - E(H_2O) + \Delta E_{ZPE} - T\Delta S \quad (5)$$

*(4)* $HOO^* \rightarrow O_2\ (g) + H^+ + e^-$

$$\Delta G_4 = E_* - E_{OOH*} + 2 \cdot E(H_2O) - 3/2 \cdot E(H_2) + 4.92 + \Delta E_{ZPE} - T\Delta S \quad (6)$$

The free energies for separating $H_2$ and $H_2O$ molecules are represented in the equation, denoted by $E(H_2)$ and $E(H_2O)$ respectively. $E_*$, $E_{OH*}$, $E_{O*}$, and $E_{OOH*}$ stand for the free energies for the bare surface and adsorbed *OH**, *O**, and *OOH** species on the surface. Adapted from the literature, the zero-point energy (ZPE) corrections $\Delta E_{ZPE}$ and $T\Delta S$ for various adsorbates at 298 K.[4]

**HER calculation:** It is consistent with the calculation parameters of OER. In the calculation for HER, the model structures of $Co(OH)_2$, Cu-$Co(OH)_2$, and $CeO_2$-$Co(OH)_2$ were optimized. The k point of the Brillouin zone is 1×1×1, and the vacuum layer thickness of all

slab models is maintained at 15 Å. The Gibbs free energy of absorption H* ($\Delta G_{H^*}$) is calculated with the following equation:

$$\Delta G_{H^*} = \Delta E_{H^*} + \Delta E_{ZPE} - T\Delta S \quad (7)$$

Here, $\Delta E_{H^*}$ represents the hydrogen adsorption energy, $\Delta E_{ZPE}$ denotes the difference in zero-point energy between adsorbed hydrogen and hydrogen in the gas phase, and $\Delta S$ indicates the hydrogen entropy difference between the adsorbed state and the gas phase. Nørskov et al. reported that the value of $\Delta E_{ZPE} - T\Delta S$ is approximately 0.24 eV in the standard case.

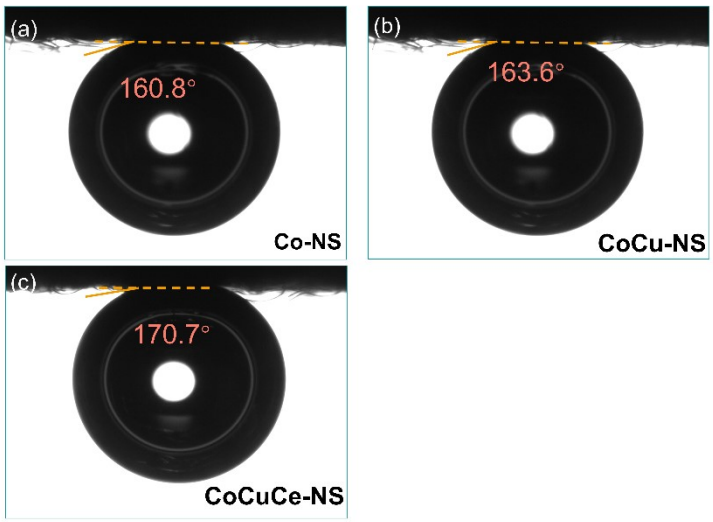


Fig. S1 The underwater bubble contact angles of (a) Co-NS; (b) CoCu-NS; and (c) CoCuCe-NS.

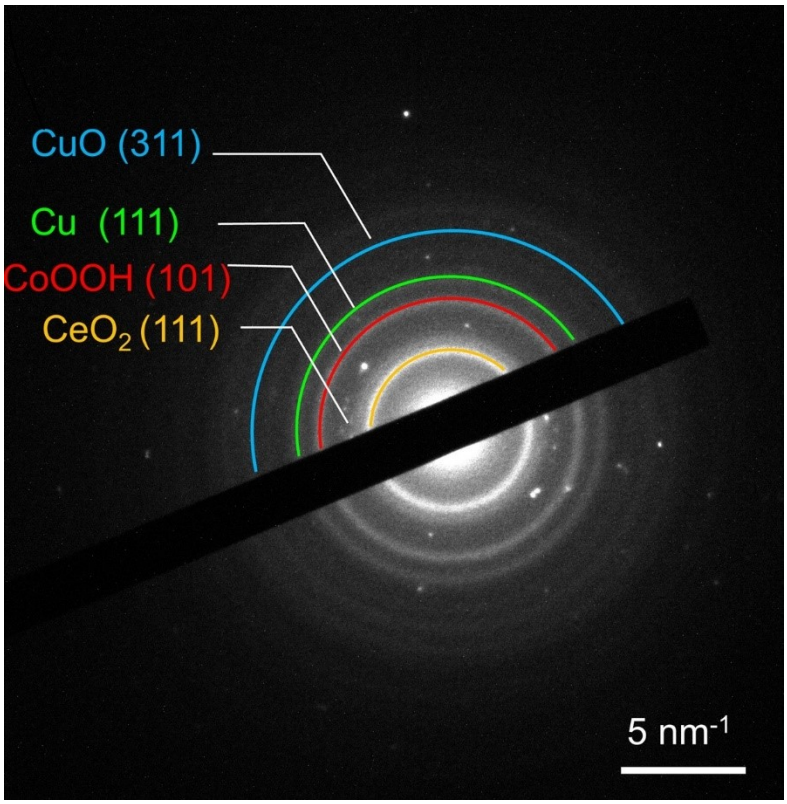


Fig. S2 The selected area electron diffraction pattern of CoCuCe-NS.

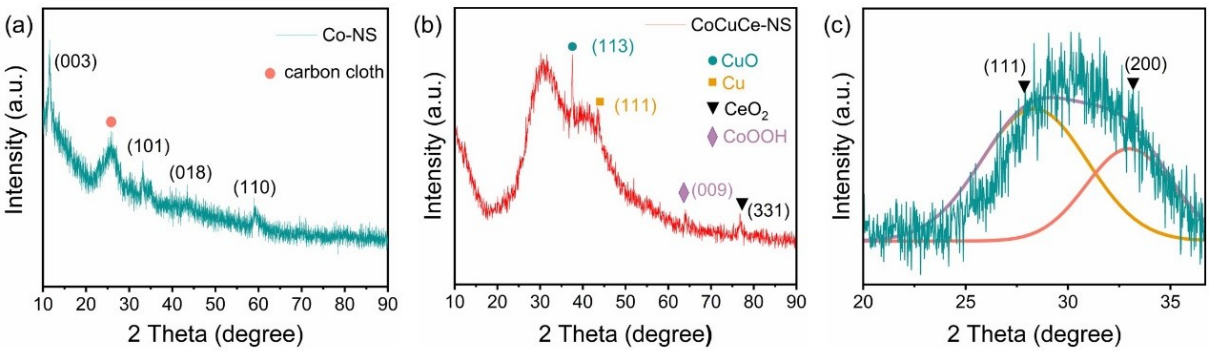


Fig. S3 XRD patterns of (a) Co-NS; (b) CoCuCe-NS. (c) interval amplification XRD pattern in Fig. (b).

Fig. S3c is a part of Fig. S3b. The peak segmentation is performed on the amplification interval, and the Gaussian peak shape is adopted after deducting the baseline.

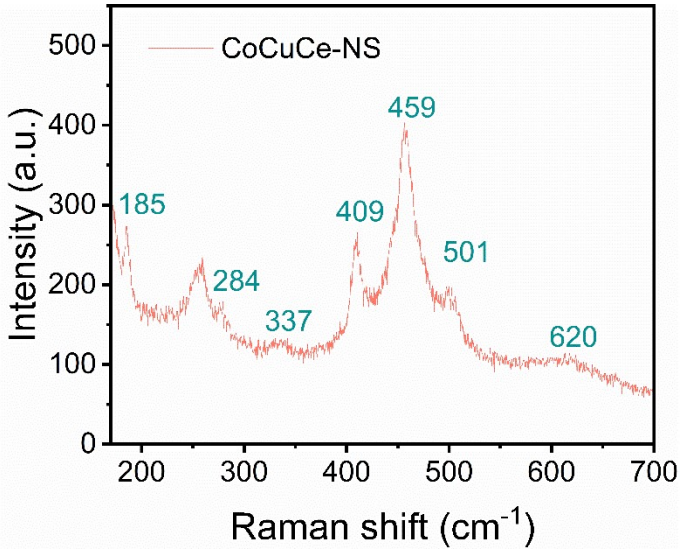


Fig. S4 Raman spectrum of CoCuCe-NS sample. In the Raman shift region between 170 to 700 $cm^{-1}$.

The peaks located at ca.185 $cm^{-1}$ and 459 $cm^{-1}$ are identified as vibrational modes of $CeO_2$, and the three vibrational modes of CuO are assigned to $A_g$, $B_g^1$, and $B_g^2$ at 284 $cm^{-1}$, 337 $cm^{-1}$, and 620 $cm^{-1}$, respectively.[5, 6] The characteristic peak appearing at 409 $cm^{-1}$ is attributed to the Cu-O model.[7] In addition, the weak peak at 501 $cm^{-1}$ contributes to the vibration of CoOOH.[7, 8]

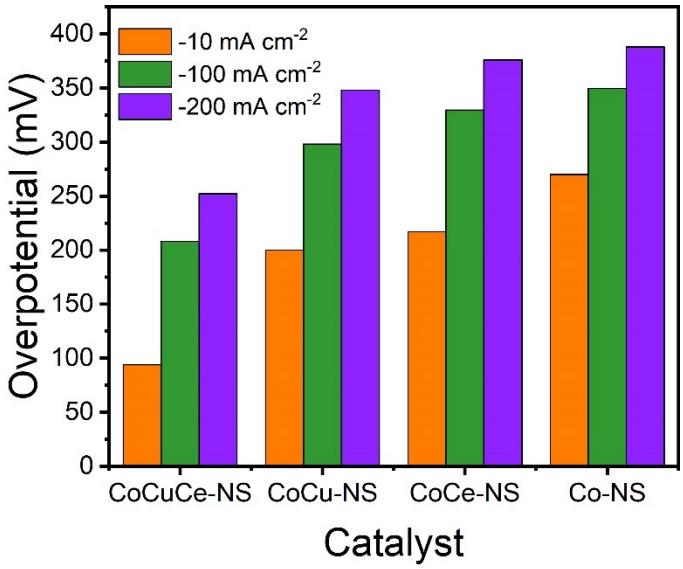


Fig. S5 The overpotential of Co-NS, CoCu-NS, CoCe-NS, and CoCuCe-NS catalysts at different current densities (HER).

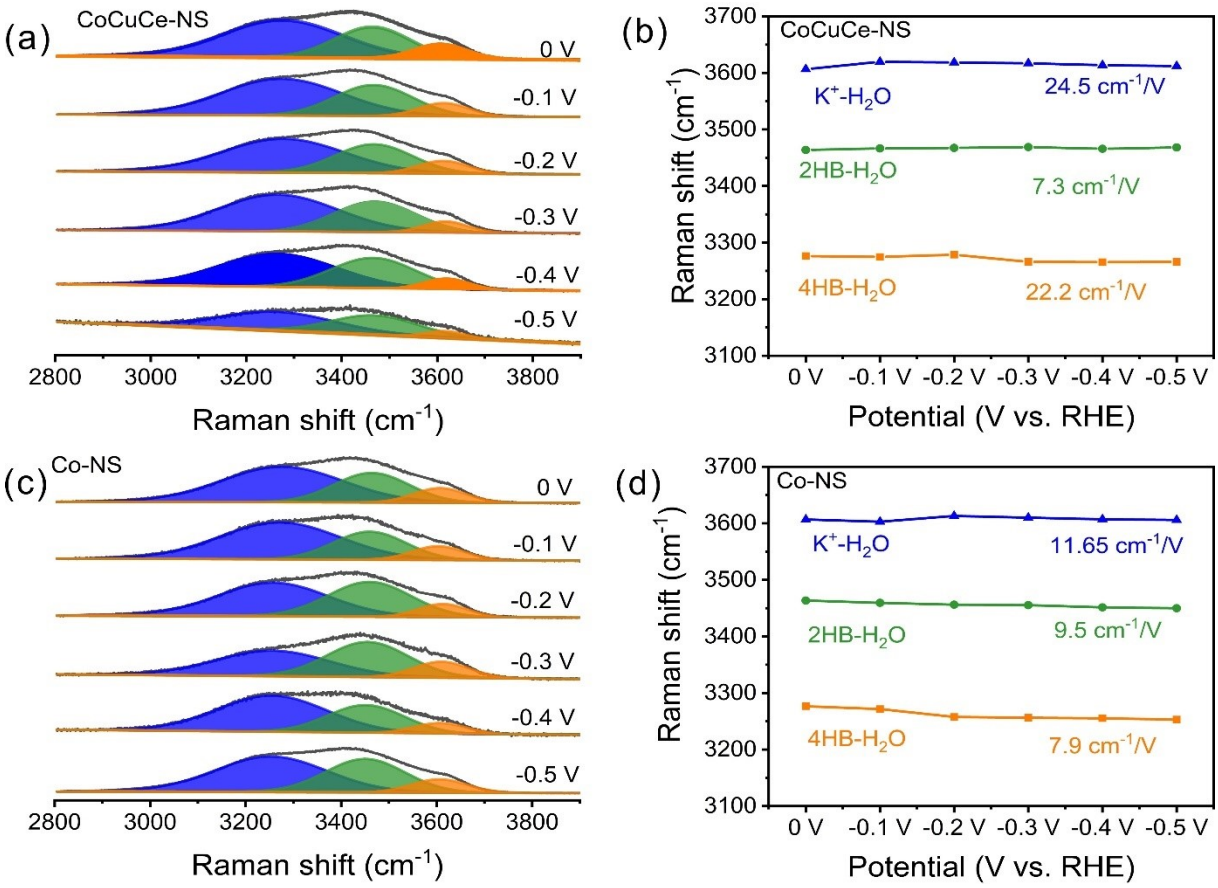


Fig. S6 Behavior of interfacial water on catalysts. In situ Raman spectra of interfacial water at (a) CoCuCe-NS and (c) Co-NS. The 4HB-$H_2O$ (blue area), 2HB-$H_2O$ (green area), and $K^+$-$H_2O$ (yellow area) show three types of O-H stretching modes. Stark tuning rates of the $\nu_{O\text{-}H}$ of interfacial water at (b) CoCuCe-NS and (d) Co-NS.

As the behavior of interfacial water on the electrocatalyst decides the Volmer process, in situ Raman spectroscopy was performed to analyze the catalytic mechanism of water dissociation for CoCuCe-NS (Fig. S6). A Gaussian fitting was performed to the broad Raman band (3000-3700 $cm^{-1}$) attributed to the O-H stretching mode ($\nu_{O\text{-}H}$) of the interfacial water. As shown in Figs. S6a and 6c, it was decomposed into three components representing different types of interfacial water: 4HB-$H_2O$, 2HB-$H_2O$, and $K^+$-$H_2O$. Resolving the effect of the local electric field on the adsorption behavior of adsorbents by studying the vibrational Stark effect. The Stark tuning values of CoCuCe-NS are 24.5 ($K^+$-$H_2O$), 7.3 (2HB-$H_2O$), 22.2 $cm^{-1}$ $V^{-1}$ (4HB-$H_2O$) while those Co-NS are 11.6, 9.5, 7.9 $cm^{-1}$ $V^{-1}$, respectively (Figs.S6b and S6d). The tuning rate value of $K^+$-$H_2O$ in CoCuCe-NS is higher than that of Co-NS, which indicates that the interaction between CoCuCe-NS and interfacial water is stronger and more conducive to O-H bond breaking. Therefore, Cu and $CeO_2$ can accelerate the adsorption/dissociation process of water molecules at the Co sites.

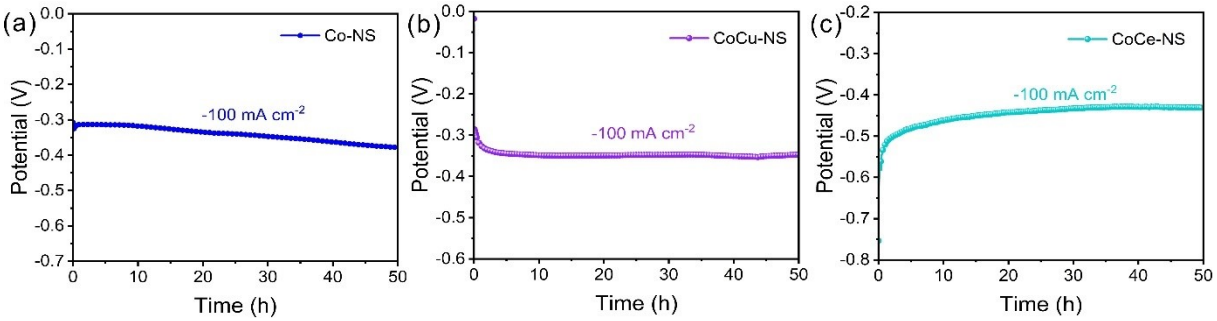


Fig. S7 Chronoamperometry measurements of long-term stability test of Co-NS, CoCu-NS, and CoCe-NS catalysts under the current density of -100 mA $cm^{-2}$.

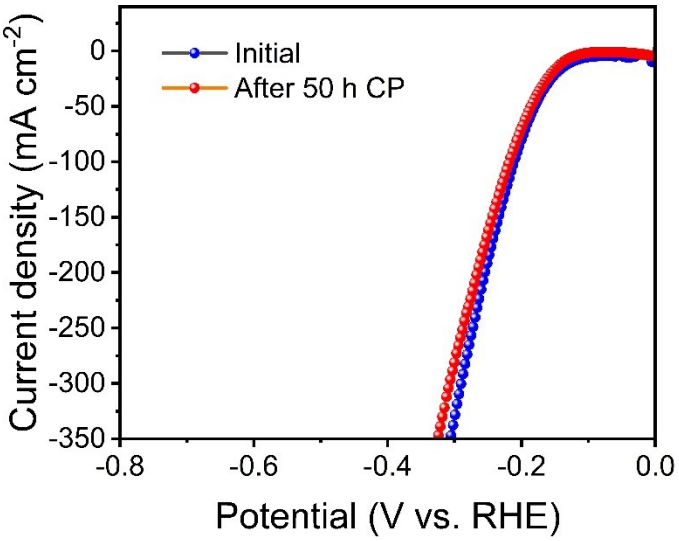


Fig. S8 Polarization curves of CoCuCe-NS before and after the 50-hour CP test at a current density of -100 mA $cm^{-2}$.

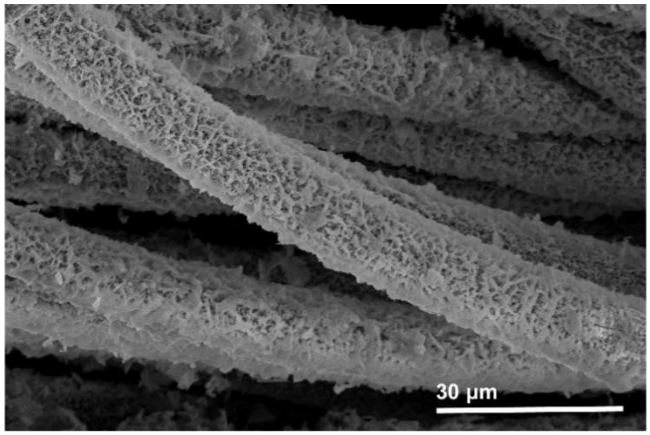


Fig. S9 SEM image of CoCuCe-NS after long-term stability testing during HER.

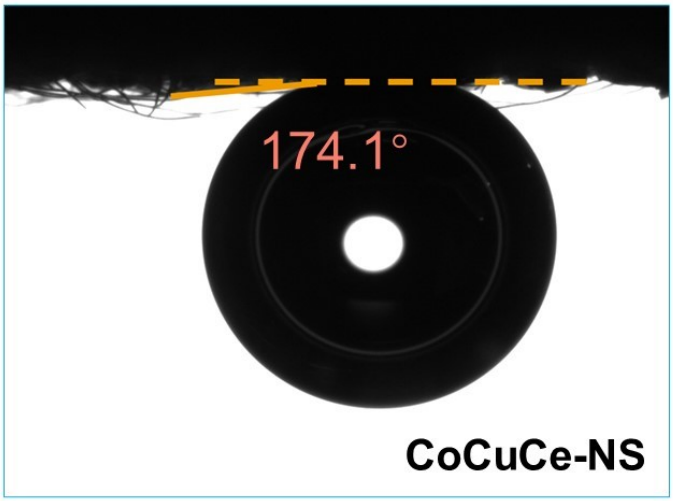


Fig. S10 The underwater bubble contact angle of CoCuCe-NS after 10 hours of long-term stability testing during HER.

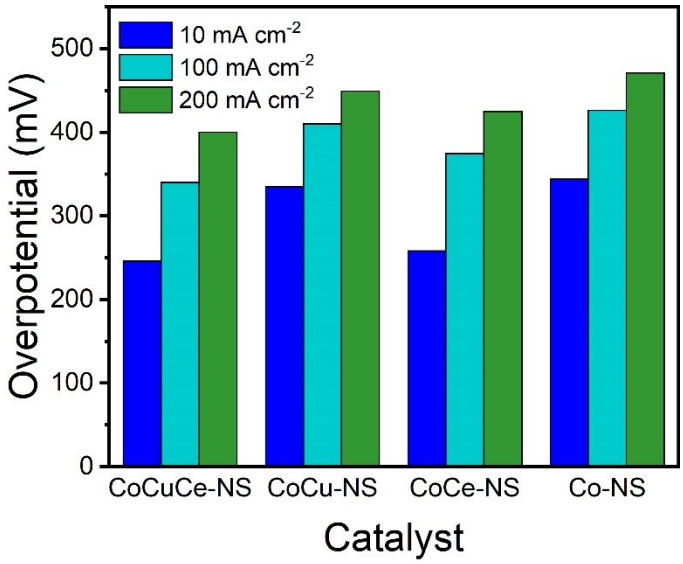


Fig. S11 The overpotential of Co-NS, CoCu-NS, CoCe-NS, and CoCuCe-NS catalysts at different current densities (OER).

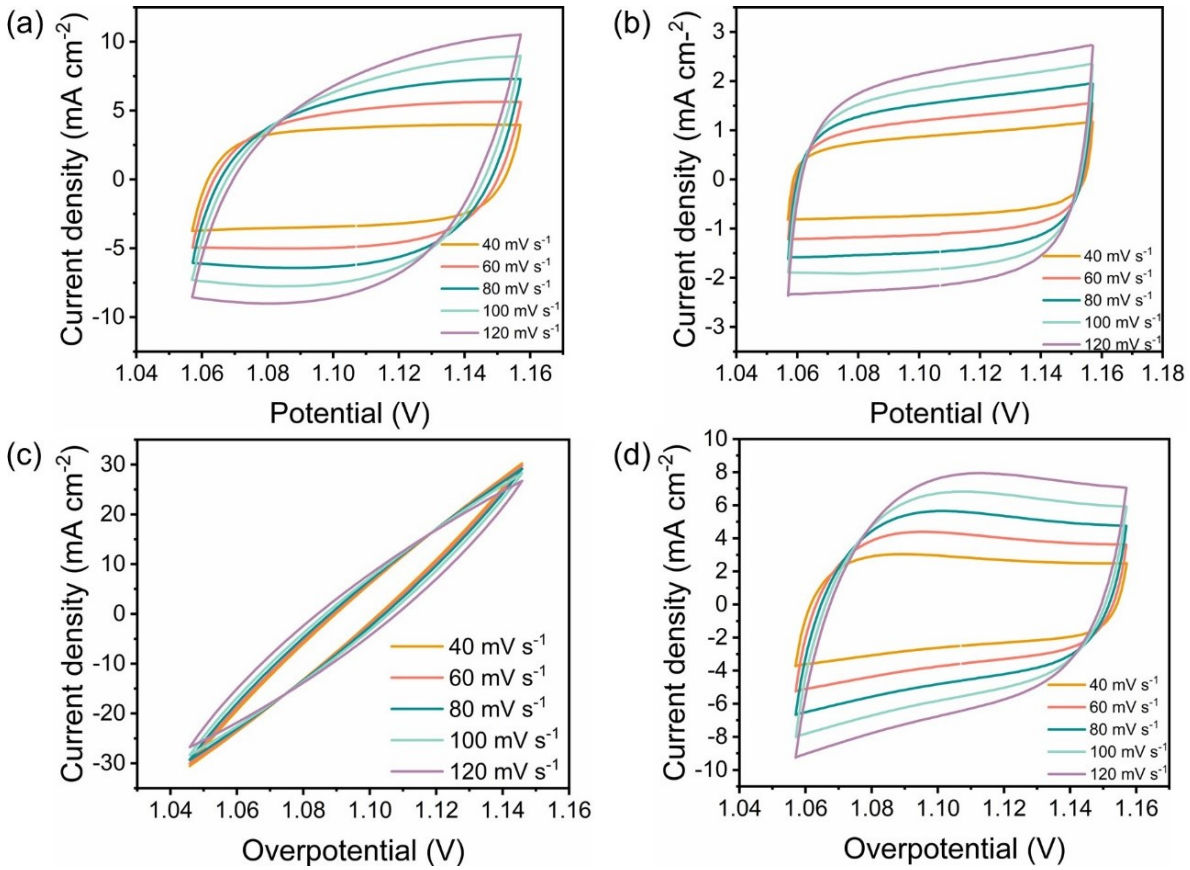


Fig. S12 Cyclic voltammetry curves of (a) Co-NS; (b) CoCu-NS; (c) CoCe-NS; and (d) CoCuCe-NS for OER in 1 M KOH with scan rates in the range of 40-120 mV $s^{-1}$.

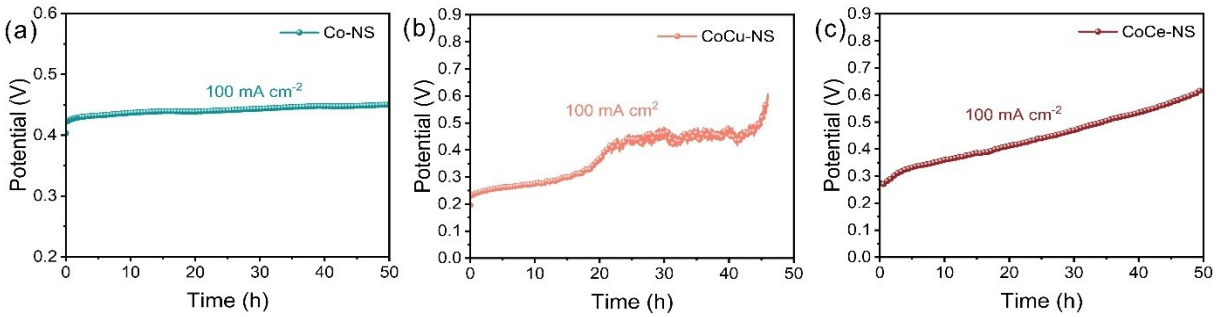


Fig. S13 Chronoamperometry measurements of long-term stability test of Co-NS, CoCu-NS, and CoCe-NS catalysts under the current density of 100 mA $cm^{-2}$.

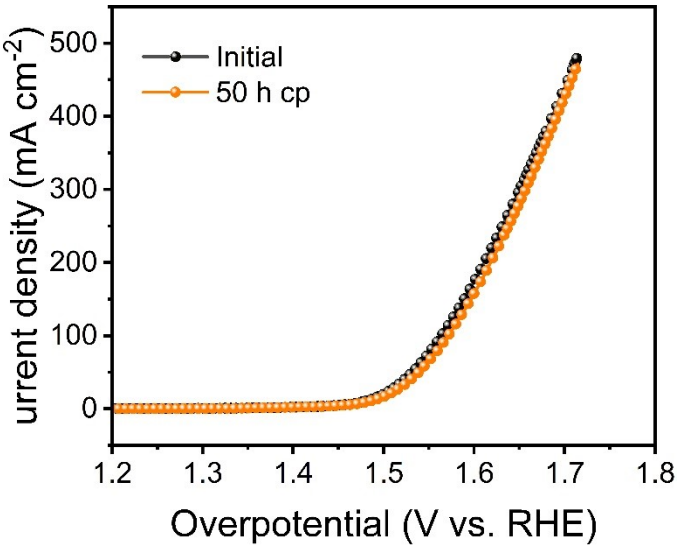

Fig. S14 Polarization curves of CoCuCe-NS before and after 50-hour CP test at a current density of 100 mA $cm^{-2}$.

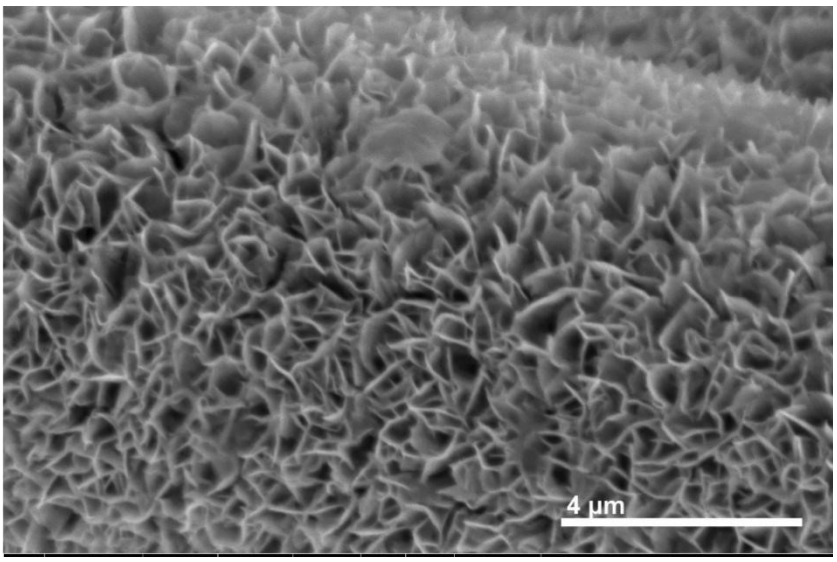


Fig. S15 SEM image of CoCuCe-NS after long-term stability testing during OER.

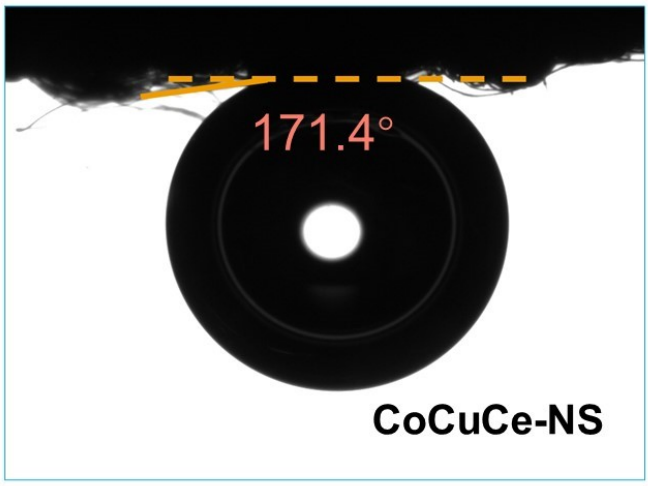


Fig. S16 The underwater bubble contact angle of CoCuCe-NS after 10 hours of long-term stability testing during OER.

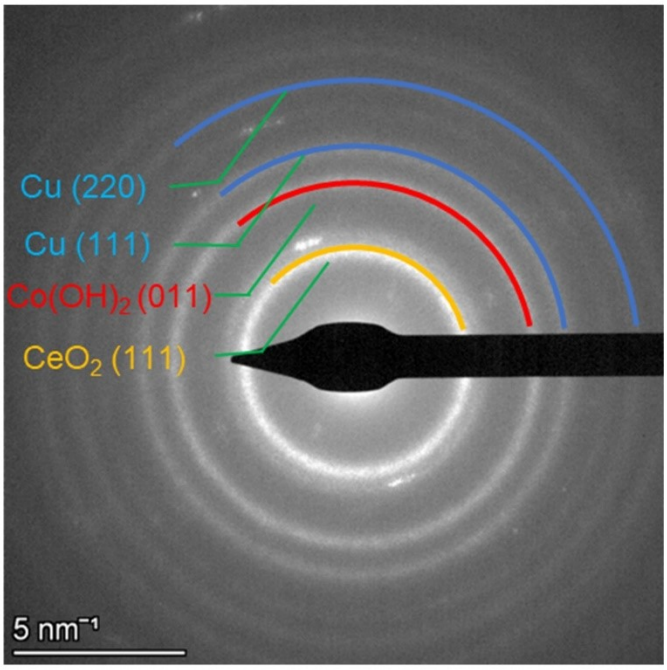


Fig. S17 SAED diagram of CoCuCe-NS after 1 hour CP treatment under the current density of -10 mA $cm^{-2}$.

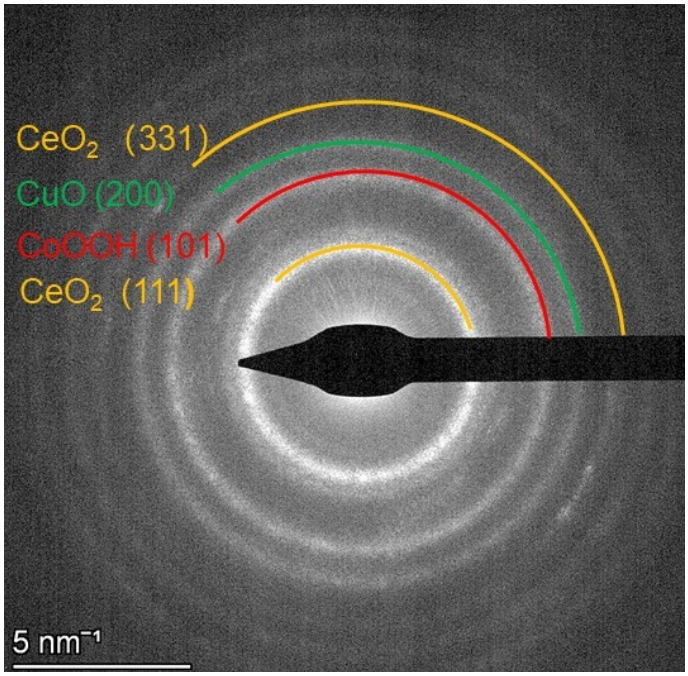


Fig. S18 SAED diagram of CoCuCe-NS after 1 hour CP treatment under the current density of 10 mA $cm^{-2}$.

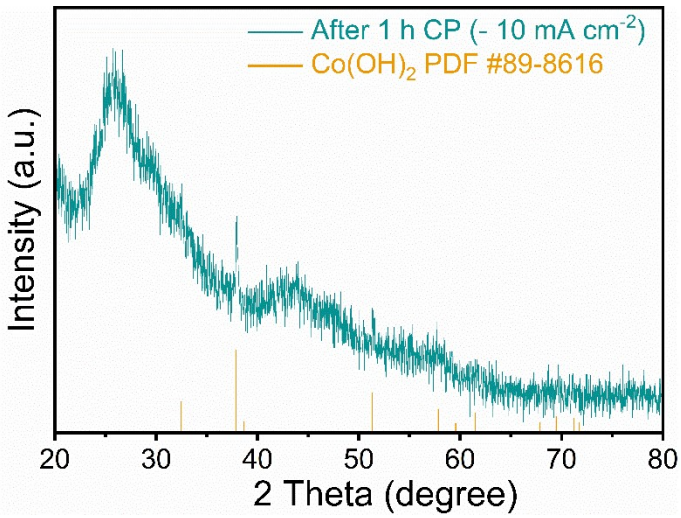


Fig. S19 X-ray diffraction patterns of CoCuCe-NS after 1 hour CP under the current density of -10 mA $cm^{-2}$.

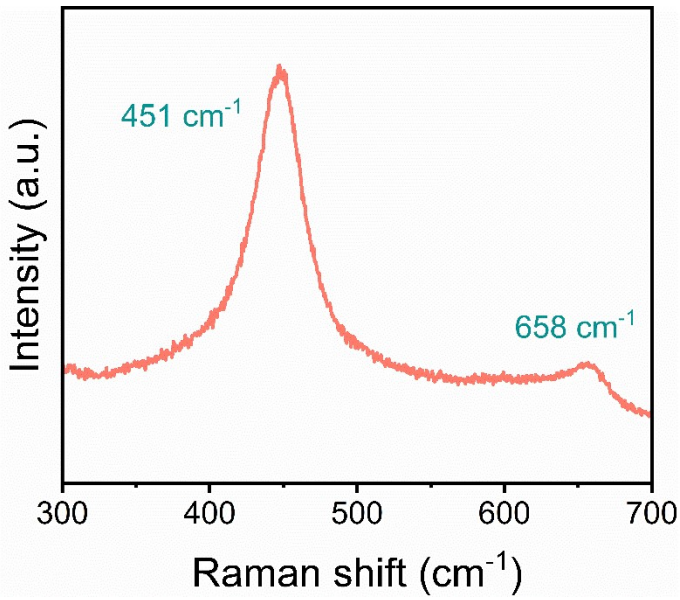


Fig. S20 Raman spectrum of CoCuCe-NS sample after 1 hour CP under the current density of -10 mA $cm^{-2}$.In the Raman shift region between 300 to 700 $cm^{-1}$.

The characteristic peaks at 451 $cm^{-1}$ and 658 $cm^{-1}$ correspond to the active vibration mode of $F_{2g}$ of $CeO_2$ and the stretching vibration of $Co^{2+}$-O, respectively.[9]

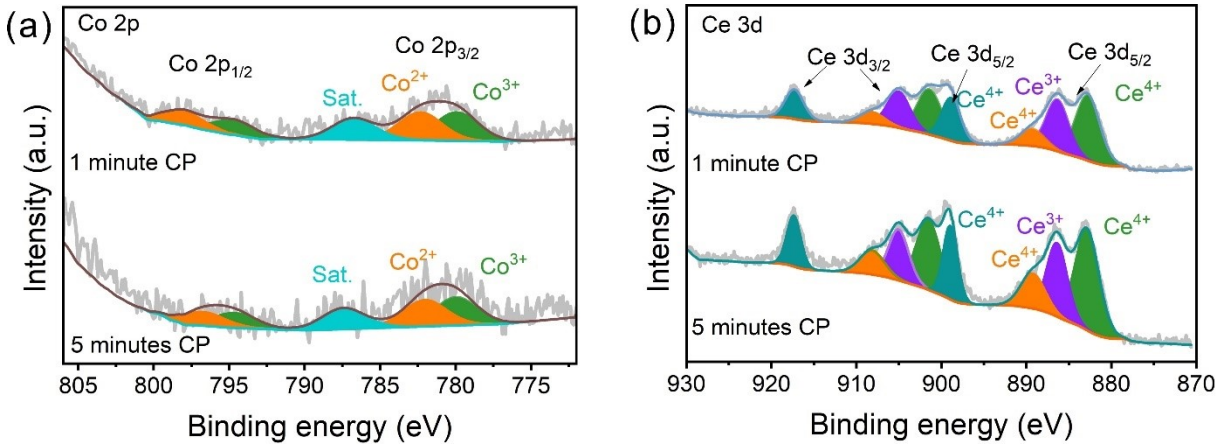


Fig. S21 (a) Co 2p and (b) O 1s high-resolution XPS spectra of CoCuCe-NS after 1 minute and 5 minutes CP under the current density of -10 mA $cm^{-2}$.

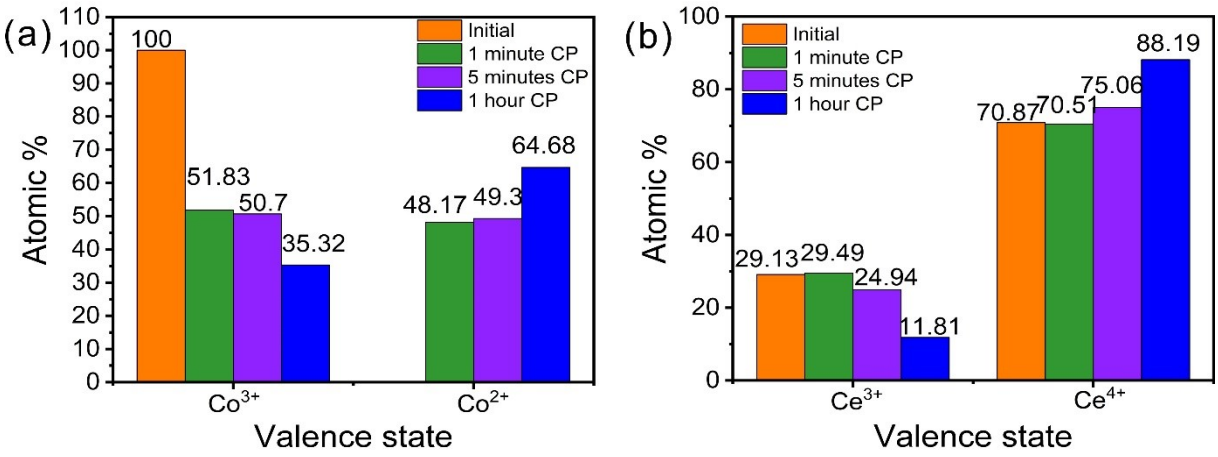


Fig. S22 Percentage of $Co^{2+}/Co^{3+}$ and $Ce^{3+}/Ce^{4+}$ tested for CP at different times under the current density of -10 mA $cm^{-2}$.

The above percentage results are derived from fitting the XPS spectra of Co 2p and Ce 3d.

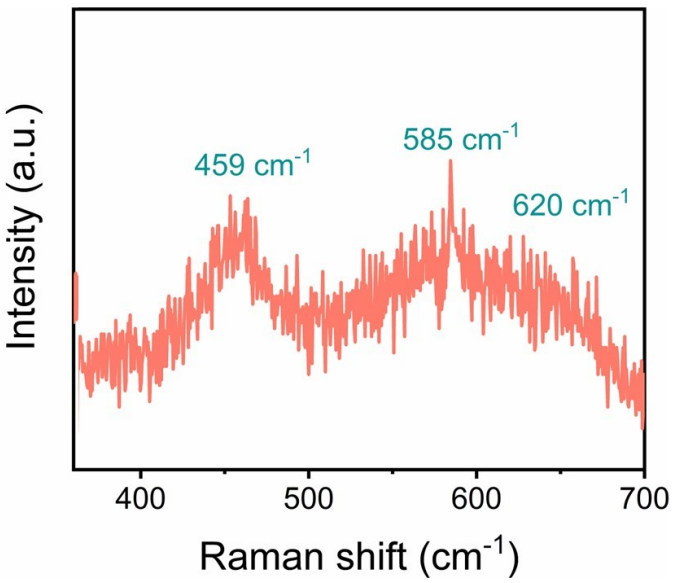


Fig. S23 Raman spectrum of CoCuCe-NS sample after 1 hour CP under the current density of 10 mA $cm^{-2}$. In the Raman shift region between 360 to 700 $cm^{-1}$.

The characteristic peaks at 585 $cm^{-1}$ correspond to the stretching vibration of O-Co-O.[9]

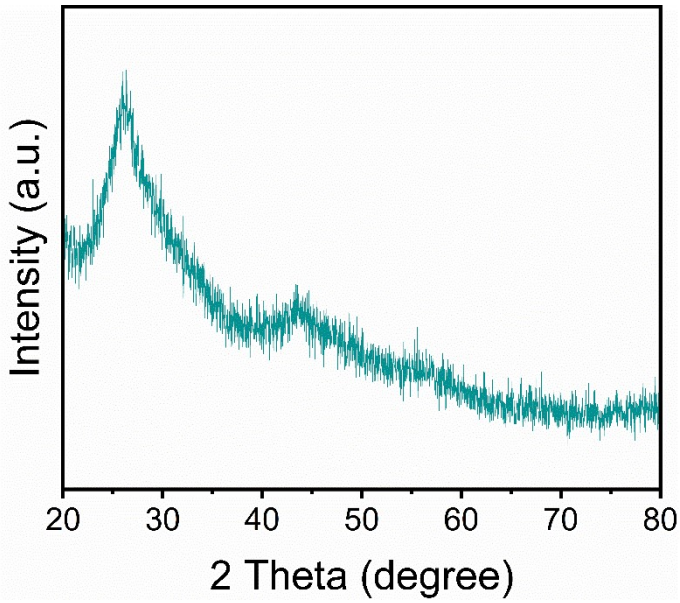


Fig. S24 X-ray diffraction patterns of CoCuCe-NS after 1 hour CP under the current density of 10 mA $cm^{-2}$.

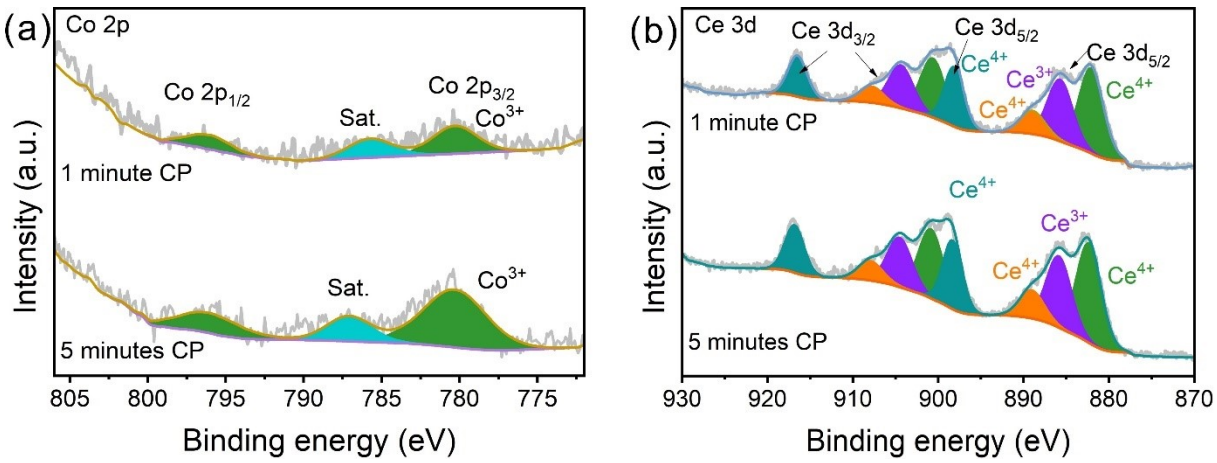


Fig. S25 (a) Co 2p and (b) O 1s high-resolution XPS spectra of CoCuCe-NS after 1 minute and 5 minutes CP under the current density of 10 mA $cm^{-2}$.

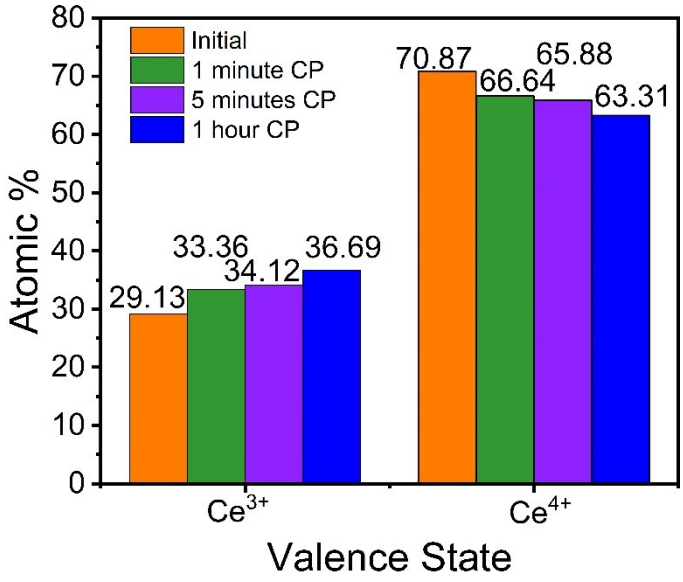


Fig. S26 Percentage of $Ce^{3+}$/$Ce^{4+}$ tested for CP at different times under the current density of 10 mA $cm^{-2}$.

The above percentage results are derived from fitting the XPS spectra of Ce 3d.

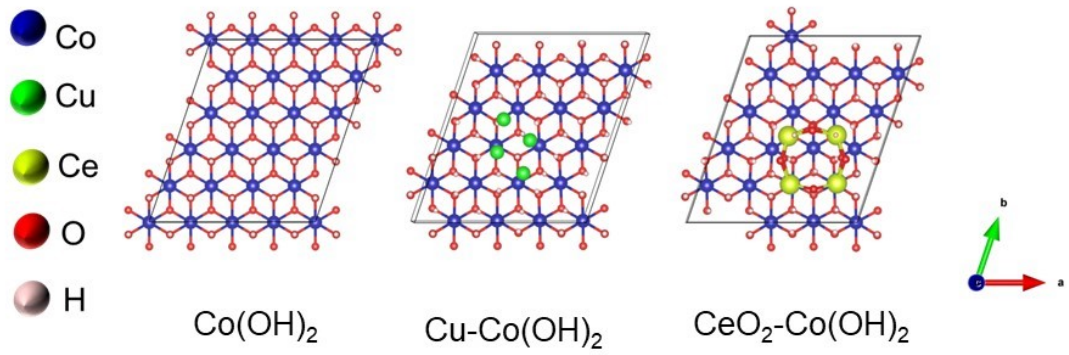


Fig. S27 The optimized model structure diagrams of $Co(OH)_2$, Cu-$Co(OH)_2$, and $CeO_2$-$Co(OH)_2$.

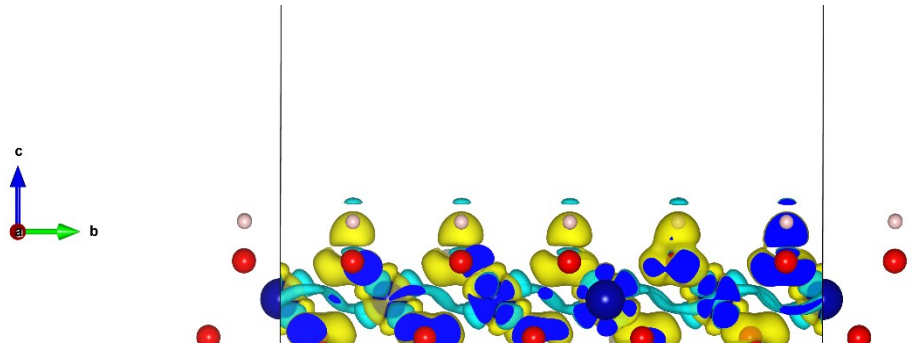


Fig. S28 The differential charge density image of $Co(OH)_2$. The yellow and blue zones represent the charge accumulation and charge consumption.

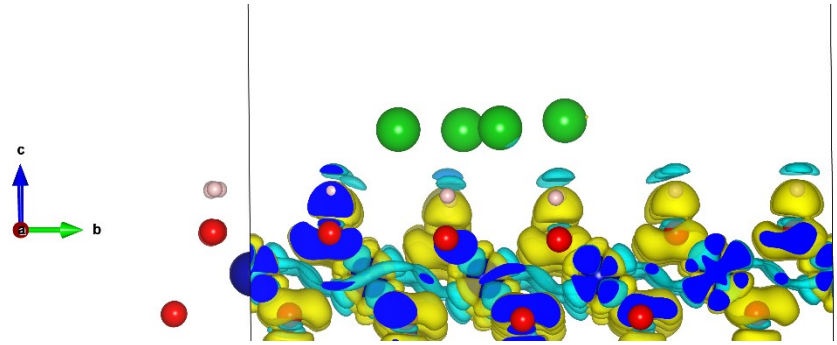


Fig. S29 The differential charge density image of Cu-$Co(OH)_2$. The yellow and blue zones represent the charge accumulation and charge consumption.

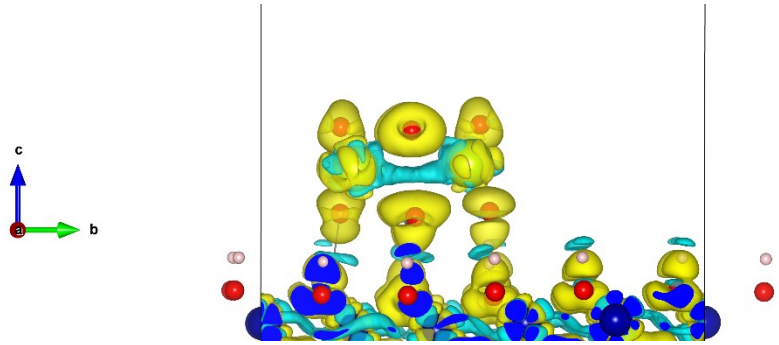


Fig. S30 The differential charge density image of $CeO_2$-$Co(OH)_2$. The yellow and blue zones represent the charge accumulation and charge consumption.

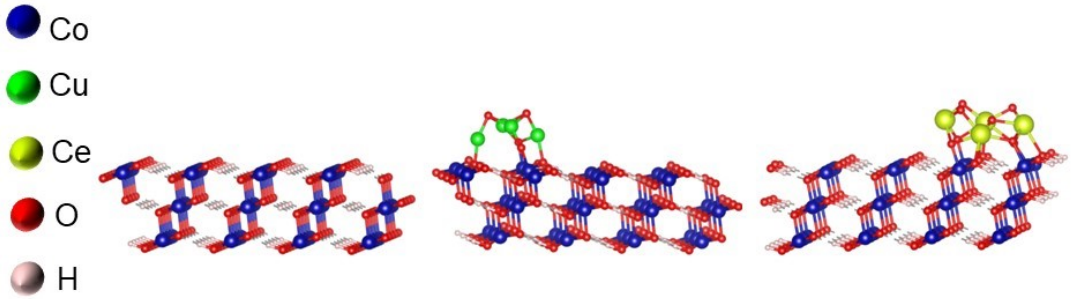


Fig. S31 The optimized model structure diagrams of CoOOH, CuO-CoOOH, and $CeO_2$-CoOOH.

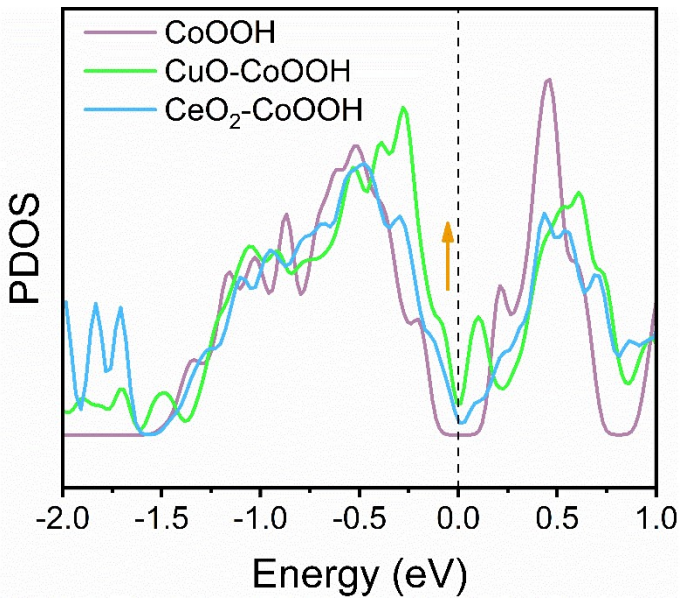


Fig. S32 The partial density of states plots of O-2*p* orbitals for CoOOH, CuO-CoOOH, $CeO_2$-CoOOH.

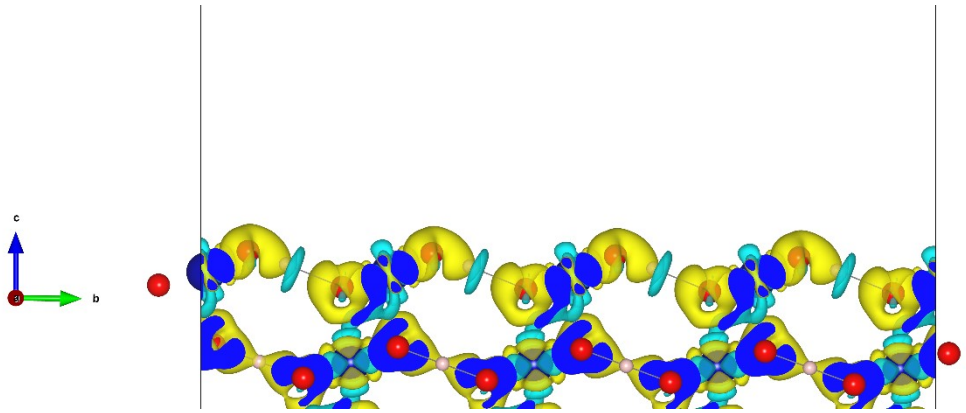


Fig. S33 The differential charge density image of CoOOH. The yellow and blue zones represent the charge accumulation and charge consumption.

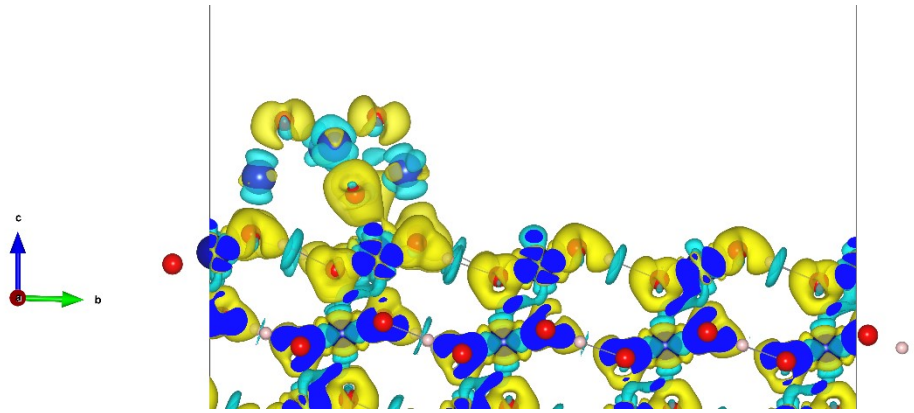


Fig. S34 The differential charge density image of CuO-CoOOH. The yellow and blue zones represent the charge accumulation and charge consumption.

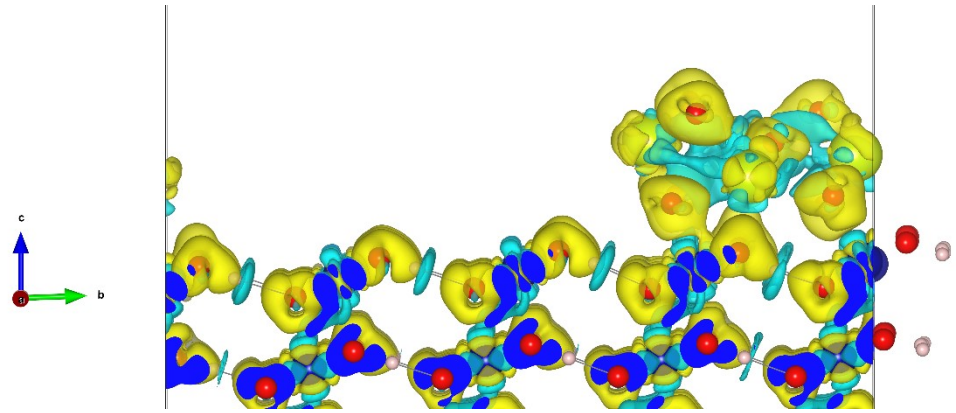


Fig. S35 The differential charge density image of $CeO_2$-CoOOH. The yellow and blue zones represent the charge accumulation and charge consumption.

Table S1. Comparison of electrochemical activity of CoCuCe-NS to the other reported HER catalysts or OER catalysts in alkaline electrolyte

| | Overpotential ($\eta_{10}$ /mV) | | |
|---|---|---|---|
| Electrocatalyst | HER | OER | Reference |
| CoCuCe-NS | 94 | 246 | This work |
| CoOOH nanosheet | | 426 | [10] |
| S-CoOOH | | 374 | [11] |
| γ-CoOOH | | 300 | [12] |
| Ru-CoOOH | | 264 | [13] |
| CoOOH/Cu/Ni foam | | 260 | [14] |
| Fe-CoOOH/G | | 330 | [15] |
| $Fe_{0.33}Co_{0.67}OOH$ PNSAs/CFC | | 266 | [16] |
| LC-CoOOH NAs/CFC | | 294 | [17] |
| Mo-CoOOH | | 305 | [3] |
| $CeO_2/Co(OH)_2$ | 317 | 410 | [18] |
| EO/Cl -doped $Co(OH)_2$ | | 330 | [19] |
| Ru/$Co(OH)_2$ NWAS | 96 | | [20] |
| Pt/Nb-$Co(OH)_2$ | 112 | | [21] |
| CoSe/$Co(OH)_2$-CM (AE) | 207 | 299 | [22] |
| $Co(OH)_2$/Ag/FeP | 118 | 236 | [23] |
| $Fe(OH)_x$@Cu-MOF | 112 | | [24] |
| $Cu_{0.3}Co_{2.7}P$/NC | 220 | 190 | [25] |
| CoNiFeCu | | 291.5 | [26] |
| NiYCe-MOF/NF | 136 | 245 | [27] |
| $Co_{1-y}Ce_yO_x$ | | 320 | [28] |
| $Ce_1$-CoP | 144 | 270 | [29] |
| Ce/N-NiO | | 250 | [30] |

**Reference**


1. Y. S. Park, J. Yang, J. Lee, M. J. Jang, J. Jeong, W.-S. Choi, Y. Kim, Y. Yin, M. H. Seo, Z. Chen and S. M. Choi, Appl. Catal. B Environ., **2020**, 278, 119276.
2. J. K. Nørskov, T. Bligaard, A. Logadottir, J. R. Kitchin, J. G. Chen, S. Pandelov and U. Stimming, J. Electrochem. Soc., **2005**, 152, J23.
3. C. Guan, W. Xiao, H. Wu, X. Liu, W. Zang, H. Zhang, J. Ding, Y. P. Feng, S. J. Pennycook and J. Wang, Nano Energy, **2018**, 48, 73-80.
4. M. Li, L. Zhang, Q. Xu, J. Niu and Z. Xia, J. Catal., **2014**, 314, 66-72.
5. C. Rosmini, T. Tsoncheva, D. Kovatcheva, N. Velinov, H. Kolev, D. Karashanova, M. Dimitrov, B. Tsyntsarski, D. Sebastián and M. J. Lázaro, Carbon, **2022**, 196, 186-202.
6. J. Zhang, K. Wu, J. Xiong, Q. Ren, J. Zhong, H. Cai, H. Huang, P. Chen, J. Wu, L. Chen, M. Fu and D. Ye, Appl. Catal. B Environ., **2022**, 316, 121620.
7. W. He, J. Zhang, S. Dieckhöfer, S. Varhade, A. C. Brix, A. Lielpetere, S. Seisel, J. R. C. Junqueira and W. Schuhmann, **Nat. Commun.**, 2022, 13, 1129.
8. W. H. Lee, M. H. Han, Y.-J. Ko, B. K. Min, K. H. Chae and H.-S. Oh, Nat. Commun., **2022**, 13, 605.
9. P. Gao, Y. Zeng, P. Tang, Z. Wang, J. Yang, A. Hu and J. Liu, Adv. Funct. Mater., **2022**, 32, 2108644.
10. S. Wang, Q. Jiang, S. Ju, C. S. Hsu, H. M. Chen, D. Zhang and F. Song, Nat. Commun., **2022**, 13, 6650.
11. X. Zhang, H. Zhong, Q. Zhang, Q. Zhang, C. Wu, J. Yu, Y. Ma, H. An, H. Wang, Y. Zou, C. Diao, J. Chen, Z. G. Yu, S. Xi, X. Wang and J. Xue, Nat. Commun., **2024**, 15, 1383.
12. Z. W. Seh, J. Kibsgaard, C. F. Dickens, I. Chorkendorff, J. K. Norskov and T. F. Jaramillo, Science, **2017**, 355, eaad4998.
13. Y. Ma, Y. Ha, L. Chen, Z. An, L. Xing, Z. Wang and Z. Li, Small, 2024, 20, 2311884.
14. H.-Y. Chen, Y.-C. Chang, J.-F. Lee, C.-W. Pao, H.-C. Huang and C.-H. Wang, ACS Sustainable Chem. Eng., **2021**, 9, 12300-12310.
15. X. Han, C. Yu, S. Zhou, C. Zhao, H. Huang, J. Yang, Z. Liu, J. Zhao and J. Qiu, Adv. Energy Mater., **2017**, 7, 1602148.
16. S. H. Ye, Z. X. Shi, J. X. Feng, Y. X. Tong and G. R. Li, Angew. Chem. Int. Ed., **2018**, 57, 2672-2676.

17. S. Ye, J. Wang, J. Hu, Z. Chen, L. Zheng, Y. Fu, Y. Lei, X. Ren, C. He, Q. Zhang and J. Liu, ACS Catal., **2021**, 11, 6104-6112.
18. M.-C. Sung, G.-H. Lee and D.-W. Kim, J. Alloys Compd., **2019**, 800, 450-455.
19. Y. Kou, J. Liu, Y. Li, S. Qu, C. Ma, Z. Song, X. Han, Y. Deng, W. Hu and C. Zhong, ACS Appl. Mater. Interfaces, **2017**, 10, 796-805.
20. X. Han, Y. J. Li, X. Wang, J. T. Dong, H. M. Li, S. Yin and J. X. Xia, Int. J. Hydrogen Energy, **2024**, 51, 769-776.
21. Y. K. Tian, M. Wen, A. J. Huang, Q. S. Wu, Z. G. Wang, Q. J. Zhu, T. Zhou and Y. Q. Fu, Small, **2023**, 19, 2207569.
22. C. Gong, W. Li, Y. Lei, X. He, H. Chen, X. Du, W. Fang, D. Wang and L. Zhao, Compos. Part B Eng., **2022**, 236, 109823.
23. X. T. Ding, Y. G. Xia, Q. N. Li, S. Dong, X. L. Jiao and D. R. Chen, ACS Appl. Mater. Interfaces, **2019**, 11, 7936-7945.
24. W. Cheng, H. Zhang, D. Luan and X. W. Lou, Sci. Adv., **2021**, 7, eabg2580.
25. J. Song, C. Zhu, B. Z. Xu, S. Fu, M. H. Engelhard, R. Ye, D. Du, S. P. Beckman and Y. Lin, Adv. Energy Mater., **2016**, 7, 201601555.
26. J. Zhang, T. Quast, W. He, S. Dieckhöfer, J. R. C. Junqueira, D. Öhl, P. Wilde, D. Jambrec, Y. T. Chen and W. Schuhmann, Adv. Mater., **2022**, 34, 2109018.
27. F. Li, M. Jiang, C. Lai, H. Xu, K. Zhang and Z. Jin, Nano Lett., **2022**, 22, 7238-7245.
28. L. Pan, Q. Wang, Y. Li and C. Zhang, J. Catal., **2020**, 384, 14-21.
29. J. Li, S. Zou, X. Liu, Y. Lu and D. Dong, ACS Sustainable Chem. Eng., **2020**, 8, 10009-10016.
30. F. Yang, X. Zhang, L. Zhou, S. Lin, X. Cao, J. Jiang and X. Lu, Chem. Eng. J., **2022**, 432, 134255.